

Enhanced structural control of soft-templated mesoporous inorganic thin films by inert processing conditions

Maximiliano Jara Fornerod^a, Alberto Alvarez-Fernandez^a, Maximilian W.A. Skoda^b, Beatriz Prieto-Simon^{c,d}, Nicolas H. Voelcker^{e,f}, Marc-Olivier Coppens^a, Stefan Guldin^{a}*

^aDepartment of Chemical Engineering and Centre for Nature Inspired Engineering, University College London, Torrington Place, London, WC1E 7JE, UK.

^bISIS Pulsed Neutron and Muon Source, Rutherford Appleton Laboratory, Harwell, Oxfordshire OX11 0QX, UK.

^c Department of Electronic Engineering, Universitat Rovira i Virgili, 43007, Tarragona, Spain

^d ICREA, Pg. Lluís Companys 23, 08010, Barcelona, Spain

^e Monash Institute of Pharmaceutical Sciences, Monash University, Parkville, Victoria, 3052, Australia

^f Melbourne Centre for Nanofabrication, Victorian Node of the Australian National Fabrication Facility, Clayton, Victoria, 3168, Australia

E-mail: s.guldin@ucl.ac.uk

Keywords: thin films; mesoporous; calcination; sol-gel; block copolymers;

Mesoporous thin films are widely used for applications in need of high surface area and good mass and charge transport properties. A well-established fabrication process involves the supramolecular assembly of organic molecules (e.g. block copolymers, and surfactants) with inorganic materials obtained by sol-gel chemistry. Typically, subsequent calcination in air serves to remove the organic template and reveal the pores. A major challenge for such coatings is the anisotropic shrinkage due to the volume contraction related to solvent evaporation,

inorganic condensation, and template removal, affecting the final porosity as well as pore shape, size, arrangement and accessibility. Here, we show that a two-step calcination process, composed of high-temperature treatment in argon followed by air calcination, leads to reduced film contraction and enhanced structural control. Crucially, the formation of a transient carbonaceous scaffold enables the inorganic matrix to fully condense before template removal. The resulting mesoporous films retain a higher porosity as well as larger, more uniform pores with extended hexagonally closed-packed order. Such films present favorable characteristics for a variety of applications, such as improved mass transport of large biomolecules. This is demonstrated for the adsorption and desorption of lysozyme into the mesoporous thin films as an example of enzyme storage.

1. Introduction

Inorganic mesoporous thin films are ideally suited for applications requiring high surface area and good mass and electron transport properties, such as in gas sensors^[1,2], fuel cells^[3,4], Bragg reflectors^[5], permselective membranes^[6], dye-sensitized solar cells^[7,8], batteries^[9,10], supercapacitors^[11,12], enzyme storage^[13], electrochemical biosensing^[12,14], catalysis^[15], etc. In most cases, the interplay between porosity and pore size is crucial for their operation. However, existing fabrication processes lack fine control over these characteristics, which constrains functionality for material demands beyond a high surface area.

One of the most attractive approaches to fabricate inorganic mesoporous thin films relies on the supramolecular assembly of sol-gel precursors with organic molecules, such as block copolymers and surfactants, that self-assemble into micelles.^[16] The use of amphiphilic block copolymers (BCP) as precursors for soft templates offers several advantages over other constituents. For example, BCPs provide access to the entire mesopore size range (between 2 and 50 nm), diverse pore morphology, and various porosities by varying the length, ratio and

number of polymeric blocks.^[17–23] On the other hand, sol-gel chemistry is a versatile synthesis method that offers access to a wide library of materials, including transition metal oxides, ceramics, and glasses (e.g. aluminosilicates, Al_2O_3 , SiO_2 , TiO_2 , indium tin oxide, Nb_2O_5).^[24,25] Thin film processing typically consists of three steps.^[26] First, the BCP host and the inorganic guest materials are co-assembled in the so-called hybrid solution. Herein, the amphiphilic diblock copolymer poly(isobutylene)-*block*-poly(ethylene oxide) (PIB-*b*-PEO) and aluminosilicate nanoparticles are mixed in an azeotropic mixture of 1-butanol and toluene. In this step, the hydrophobic interactions of the PIB block with the solvent induces the BCP to self-assemble into micelles, and simultaneously the hydrophilic PEO block forms hydrogen bonds with the nanoparticles. Second, the solution is dispersed onto a substrate, generating a hybrid thin film. Third, the inorganic nanoparticles condense into an aluminosilicate network, followed by the removal of the PIB-*b*-PEO to reveal the pores.

Calcination in air is often preferred over other methods (such as oxygen plasma, solvent extraction, UV-ozone treatment) to remove the polymer from the inorganic matrix for its dual effect on the film. First, temperature induces the condensation of the inorganic component, generating a continuous solid network. Second, the oxidizing conditions degrade the BCP to reveal the pores.^[27] However, this process also has a detrimental effect on the films. Several studies have shown that the hybrid layer undergoes a uniaxial contraction of up to 70% in the direction perpendicular to the substrate, resulting in flattened pores with limited access.^[28–36] This anisotropic shrinkage is often attributed to the residual solvent evaporation and mass loss of the sol-gel during the condensation reaction,^[31,37–39] combined with a film firmly attached to the substrate.^[40] Consequently, the thin film densifies during calcination, with negative impact on both porosity and film thickness, limiting the functionality of such materials.

Processing methods to reduce the uniaxial film shrinkage of inorganic materials are limited to date. For instance, sequential deposition and annealing in a layer-by-layer approach allow to

alleviate crack formation by inducing film shrinkage during gradual layer build-up.^[39] Another processing protocol requires to pre-treat the hybrid film with liquid paraffin to stimulate the condensation of the sol-gel precursors before calcination, reducing the uniaxial contraction.^[41] In this paper, we apply a simple two-step calcination process, namely high-temperature treatment in argon, followed by air calcination, to reduce the unfavorable effects of direct thermal combustion of the templating agent on mesoporous inorganic thin films, here demonstrated for aluminosilicates. In the first step, a high temperature coupled with an inert atmosphere carbonizes the BCP, making a hard scaffold that keeps the inorganic matrix in place during the condensation reaction. In the second step, calcination in air removes the carbon scaffold from the inorganic network to reveal the mesopores. Lee *et al.* originally developed this method for bulk materials, which shrink isotropically upon condensation, to obtain mesoporous architectures with a solid crystalline wall structure while avoiding the destruction of the pores caused by the temperatures necessary to induce crystallization.^[42] To the best of our knowledge, the effect of such a processing approach on the mesoporous properties of thin films has not been studied yet. We apply a range of analytical tools, including spectroscopic ellipsometry (SE), environmental ellipsometric porosimetry (EEP), Fourier-Transform Infrared (FTIR) spectroscopy, grazing-incidence small-angle scattering (GISAXS), and scanning electron microscopy (SEM) to track structural parameters at processing steps and identify an ideal experimental procedure to exploit transient carbon scaffolding for improved structural control in mesoporous thin film architectures. Finally, we use a quartz crystal microbalance (QCM) to demonstrate the benefits of the two-step processing protocol for enzyme storage applications.

2. Results and discussion

2.1. Two-step calcination protocol

Hybrid thin films were fabricated following a protocol reported elsewhere.^[17,18] In brief, a previously hydrolyzed aluminosilicate sol from aluminum-tri-sec-butoxide and (3-glycidyloxypropyl)-trimethoxysilane (GLYMO) were mixed with the structure-directing agent PIB-*b*-PEO prior to thin film deposition by spin coating. The hybrid films were subsequently annealed in argon at a temperature of 450 °C. Under such inert conditions, the thermally stable sp²-hybridized carbon of the hydrophobic polymeric PIB block is expected to convert into a carbonaceous residue.^[42] Subsequently, air calcination at 450 °C was applied to remove the carbon-scaffold of the film and fully expose the mesoporous architecture. An overview of the fabrication process involving a “two-step” calcination is shown in **Figure 1**.

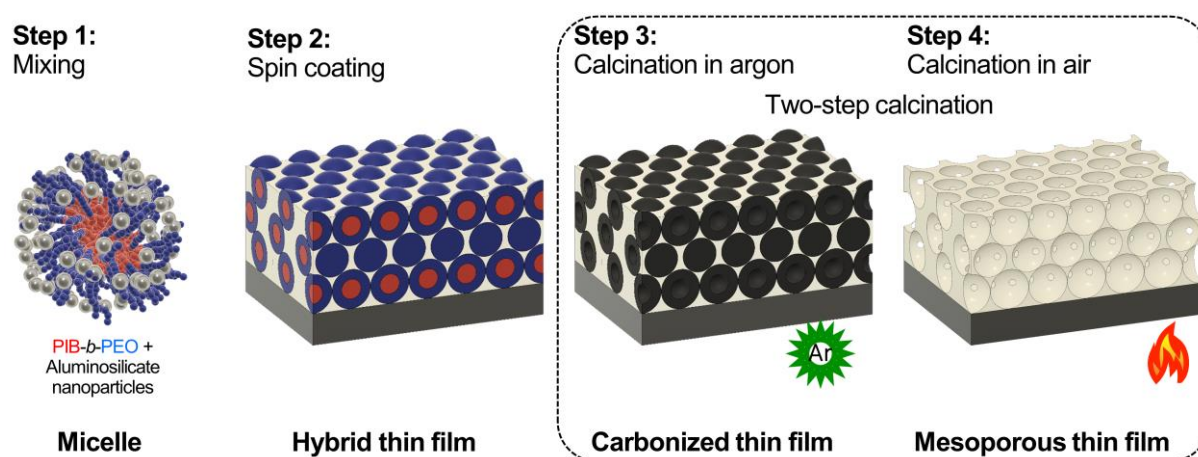


Figure 1 Schematic of the mesoporous thin film fabrication process via two-step calcination.

2.2. Effect of temperature in the fabrication of mesoporous thin films in oxidizing and inert conditions

A disadvantage of calcination procedures in air is the significant uniaxial contraction or thickness shrinkage.^[28–30] Besides the initial solvent evaporation, a well-known source of contraction in sol-gel chemistry is the mass loss due to the underlying condensation reaction.^[39] In silicates, temperature induces the condensation of silanol (Si-O-H) groups on sol particles into a continuous siloxane (Si-O-Si) network, generating water and alcohol molecules in the

process.^[43] This results in the shrinkage of the material along the silicate-rich directions, with an anisotropic effect on thin films, because they are fixed to the substrate.^[40] In order to understand the effect of temperature on the kinetics of the concurrent processes observed under oxidizing conditions, i.e. aluminosilicate sol-gel reaction and organic thermal combustion, we employed Fourier-Transform Infrared (FTIR) spectroscopy. In **Figure 2a**, the respective spectra are shown of samples treated for 30 min at temperatures ranging from 150 °C to 450 °C in air atmosphere. We use the Si-O (1120 cm^{-1}) and Al-O-Si (1220 cm^{-1}), and the C-H (2880 and 2950 cm^{-1}) stretching bands to track the condensation reaction and organic degradation, respectively (Figure 2a dashed lines i, ii, and iii). The Si-O and Al-O-Si stretching bands correspond to the inorganic network. The C-H stretching bands are the fingerprint of the organic content, in this case, PIB-*b*-PEO and residual organic molecules from the sol-gel hydrolysis. The FTIR spectrum of the sample calcined in air at 450 °C served as reference sample, where the aluminosilicate structure is fully condensed and the PIB-*b*-PEO degraded. We found that the C-H stretching band disappeared between 240 °C and 270 °C, indicating BCP degradation. In contrast, we observed the inorganic network continued evolving beyond 270 °C, as evidenced by the broadening of the Si-O stretching band. Also, a new peak emerged between 270 °C and 300 °C, which corresponds to the Al-O-Si stretching band, indicating that the aluminum starts entering the siloxane network.^[43] Please note that we did not observe changes in the Si-O stretching band at temperatures below 180 °C, which is typically referenced as suitable annealing temperature in literature.^[18,44,45] In consequence, we did not apply intermediate annealing procedures but calcined the thin films directly after spin coating.

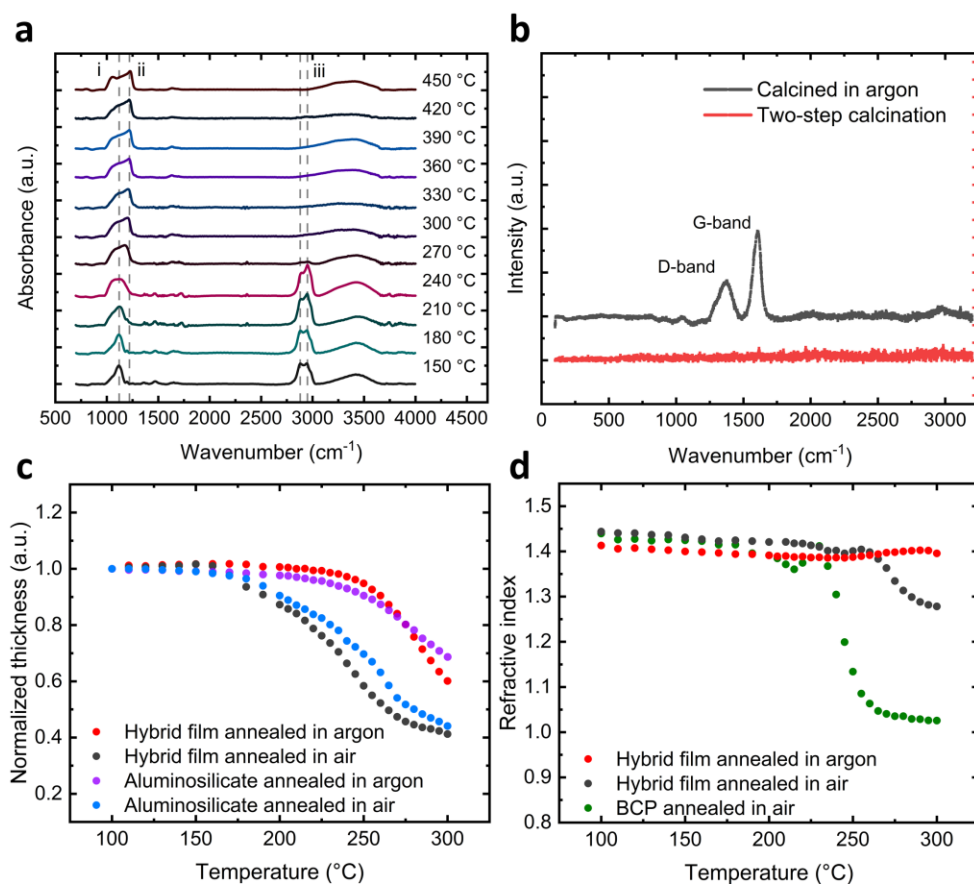


Figure 2 Hybrid thin films annealed at different temperatures. a) FTIR spectra of hybrid films annealed from 150 °C to 450 °C in air. b) Raman spectra of a carbonized hybrid film after annealing in argon at 450 °C, showing the characteristic carbon bands (D-band and G-band) and the spectra of the same film after air calcination, showing the disappearance of the carbon bands. c-d) *In situ* ellipsometric measurements showing the thickness and refractive index evolution of samples annealed in air and argon.

FTIR measurements showed that the complete degradation of the PIB-*b*-PEO occurred between 240 °C to 270 °C in samples calcined in air, while the condensation of the inorganics started at 180 °C and continued up to 450 °C. Therefore, a significant portion of the condensation, from 270 °C to 450 °C, occurred without any structural support provided by the BCP. In contrast, calcination in argon promotes the *in situ* formation of carbon species that remain in the film at this temperature, as depicted by the peaks of the disordered (D-band, 1350 cm^{-1}) and graphitic (G-band, 1600 cm^{-1}) carbon bands in the Raman spectra shown in Figure 2b.^[46]

To understand the contribution of the carbonization step to reduce the uniaxial contraction of the mesoporous film, we studied the film thickness evolution upon heating using a spectroscopic ellipsometric set-up with a temperature and atmosphere controlled chamber. We found that the thickness reduction of hybrid films annealed in argon was significantly delayed when compared with films directly annealed in air, as shown in Figure 2c by red and black dots, respectively. While at 250 °C in argon atmosphere, the hybrid films still exhibited 95% of their initial film thickness, this was already reduced to 60% in air. At 300 °C, the difference was found to be 60% vs 41%. We attributed the higher film shrinkage observed in films annealed in air up to 300 °C to the early degradation of the BCP. We also noticed that the thickness evolution for hybrid films annealed in air (Figure 2c, black dots) was similar to the thickness profile of pure aluminosilicate films annealed in air (Figure 2c, blue dots). This suggests that the BCP acts mainly as porogen in oxidizing conditions rather than to provide structural support. In contrast, annealing in argon led to a prolonged retention of the initial film thickness in a temperature range relevant for the build-up of the inorganic network, thus contributing to the structural integrity of the films.

The hybrid film can be represented as an effective medium composed of volume fractions of PIB-*b*-PEO and aluminosilicate.^[47] The refractive index of the film decreases during air calcination due to the BCP removal, which results in air-filled pores with a lower refractive index. Therefore, tracking the changes of the refractive index allows identifying the BCP degradation temperature, as shown in Figure 2d. We found that air degradation of the BCP from the hybrid film starts at ~260 °C up to ~300 °C, as depicted in Figure 2d (black dots), in line with the FTIR results discussed above. Notably, no pronounced change in the refractive index was perceived on films annealed in argon up to 300 °C (red dots), indicating that the organic material remained in the structure at this temperature range. Interestingly, the degradation of a pure BCP thin film started at ~230 °C (green dots), i.e. ~30 °C earlier than in the hybrid film.

We attribute the delay in the degradation onset to the barrier effect produced by the inorganic particles in the hybrid film, which slow down the oxygen diffusion through the material.^[48–51]

2.3. Effect of the two-step calcination on the mesoporous thin film structure

To characterize the effect of the inert processing conditions on the uniaxial film shrinkage, porosity, and pore size, we fabricated mesoporous films with 20, 30, and 40% of block copolymer content in the hybrid solution, labeled BCP₂₀, BCP₃₀, and BCP₄₀, respectively, and compared side-by-side the mesoporous structure obtained on films directly calcined in air versus two-step calcined films. We measured the film thickness by spectroscopic ellipsometry (SE) and the porosity and pore size by environmental ellipsometric porosimetry (EEP), as shown in **Figure 3**. The uniaxial contraction was calculated as the ratio of the thickness after the final calcination over the initial thickness in the hybrid state after spin coating at room temperature. We found that the two-step processed films undergo a uniaxial contraction of $62\pm3\%$, $55\pm4\%$, and $59\pm2\%$ for the samples BCP₂₀, BCP₃₀, and BCP₄₀, respectively. These values are lower than the uniaxial contraction observed on similar films directly calcined in air, i.e. $68\pm2\%$, $66\pm3\%$, and $65\pm2\%$. We classified the shape of the physisorption isotherms (Figure 3a-c) as type IV(a) and the hysteresis loop as H2b, according to the IUPAC categories.^[52] This classification is typical of mesoporous materials with ellipsoidal pores interconnected by narrow necks.^[26] The isotherm shape of the two-step calcined films is similar to that of those films directly calcined in air, indicating that the proposed two-step fabrication process has no significant effect on the interconnection of the pores. Porosity values of the films were obtained from the maximum water volume adsorbed on each isotherm. For films calcined directly in air, the porosity ranged from 42 to 66% (Figure 3a-c, black curves) for the films BCP₂₀ to BCP₄₀. Notably, the porosity was consistently higher for samples calcined in two steps, with a range of 49 to 72% (Figure 3a-c, red curves) for equivalent BCP content. Furthermore, argon-annealed

films fabricated with 40% of block copolymer led to porosities similar to the packing factor of a perfect hexagonal close-packed structure (74%).

The pore size distribution was calculated from the adsorption branch of the isotherms using the modified Kelvin equation,^[53] as depicted in Figure 3d-f. The mean pore size (D_{ads}) of the two-step calcined films was consistently larger (7.5 ± 2.2 to 13.3 ± 3.3 nm) compared to films directly calcined in air (5.8 ± 2.4 to 10.9 ± 3.5 nm) with equivalent organic content (BCP₂₀ to BCP₄₀). Hence, the uniformity of the pores markedly improved as demonstrated by the coefficient of variation, being 0.29 (BCP₂₀) and 0.25 (BCP₄₀) for the two-step calcined films in comparison to 0.41 (BCP₂₀) and 0.32 (BCP₄₀) for direct calcination.

Figure 3g-i shows the pore interconnection size distribution calculated from the desorption branch of the isotherms. The mean size of the interconnections (D_{des}) of films treated with the two-step calcination process did not exhibit a significant difference from films directly calcined in air. This suggests that the interconnectivity of the mesopores is determined by openings that are not affected by the described processing conditions.

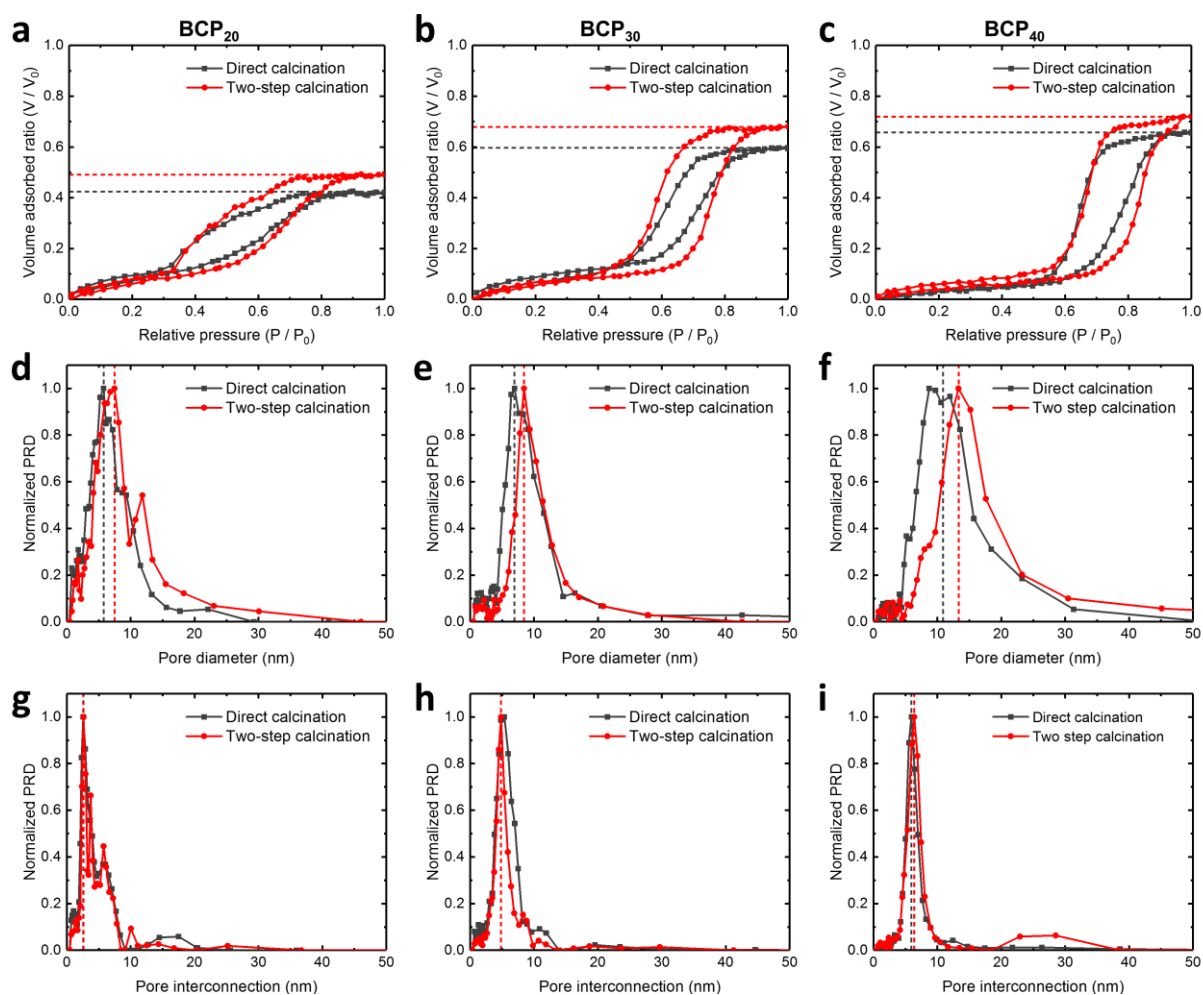


Figure 3 Environmental ellipsometric porosimetry isotherms of thin films directly calcined in air (black curves) and after two-step calcination (red curves) of a) BCP₂₀, b) BCP₃₀ and c) BCP₄₀ films alongside with their pore size distribution (d-f) and pore interconnection size distribution (g-i), respectively. Red and black dashed lines indicate the corresponding film porosity, mean pore size, and mean pore interconnection size.

In summary, thin films initially treated at elevated temperature in argon atmosphere consistently displayed an increased accessible porosity, lower shrinkage as well as bigger pore size compared to films directly calcined in air. These findings demonstrate the robustness of the method to preserve the arrangement obtained at the hybrid stage within a wide range of organic/inorganic ratio. **Table 1** summarizes all the structural parameters obtained by SE and EEP. Figure S1 in the Supplementary Information shows a graphical summary of porosity, shrinkage, and pore size. We also demonstrated the applicability of this fabrication method to

films made using the block copolymer poly(isoprene)-*b*-poly(ethylene oxide) PI-*b*-PEO with larger Mn, where the hydrophobic PI block exhibits a higher number of thermally stable sp²-hybridized carbon in comparison to PIB, obtaining similar results, as shown in the Supplementary Information Figure S2 and Figure S3.

Table 1 Thin film structural parameters obtained from the SE and EEP measurements.

Sample	Calcination process	Thickness before calcination [nm]	Thickness after calcination [nm]	Final thickness [% initial thickness]	Uniaxial contraction [%]	Porosity [vol%]	Mean pore size D _{ads} [nm]	Mean pore interconnections size D _{des} [nm]
BCP ₂₀	Two-step	177.5	67.3	37.9	62.1	49.1	7.5±2.2	2.6±0.3
BCP ₂₀	Direct	184.7	59.9	32.4	67.6	42.4	5.8±2.4	2.6±0.7
BCP ₃₀	Two-step	375.7	168.0	44.7	55.2	67.9	8.4±1.9	4.8±0.8
BCP ₃₀	Direct	380.4	130.2	34.2	65.8	59.7	6.9±2.2	4.8±1.2
BCP ₄₀	Two-step	292.2	118.6	40.6	59.4	72.0	13.3±3.3	6.4±0.9
BCP ₄₀	Direct	278.3	98.9	35.5	64.5	65.8	10.9±3.5	5.9±0.8

2.4. Effect of the two-step calcination in the mesoporous order

Grazing incidence small-angle X-ray scattering (GISAXS) is a non-destructive characterization technique that allows obtaining structural information from the mesoporous thin film such as the packing structure, center-to-center distance (D_{C-C}) and order domains.^[54] Since the footprint of the X-ray beam at grazing incidence is typically of several mm², GISAXS provides structural information over a relatively large sample area, compared to atomic force or scanning electron microscopy. **Figure 4** shows the scattering patterns for films calcined only in air and via the two-step protocol, respectively. The integration of the GISAXS line cutting along the in-plane direction (q_y) provides information of the horizontal mesopore arrangement (Figure 4 e-f). We consistently found that two-step thin films exhibited in-plane a long-range hexagonal close-packed (HCP) mesoporous order, as depicted by the peaks in the angular positions 1, $\sqrt{3}$ and $\sqrt{4}$.^[55] This was in contrast to the single peak observed for samples directly calcined in air. The

line cut integration in the out-plane direction (q_z) (see Supplementary Information Figure S4) shows that the transversal periodicity was not disturbed by the processing. These results indicate that the uniaxial contraction led to an increased disorder of the pore arrangement, breaking the HCP symmetry obtained in the hybrid state. Hence, the two-step calcination contributes to retain the horizontal mesopore periodicity by reducing the displacement induced by the shrinkage. Consistently, we found that horizontal extent of order, i.e. the Scherrer domain size^[56] calculated from the first peak (q^*) normalized by the in-plane D_{C-C} , was larger for all the two-step calcined samples compared with their air-calcined pairs.

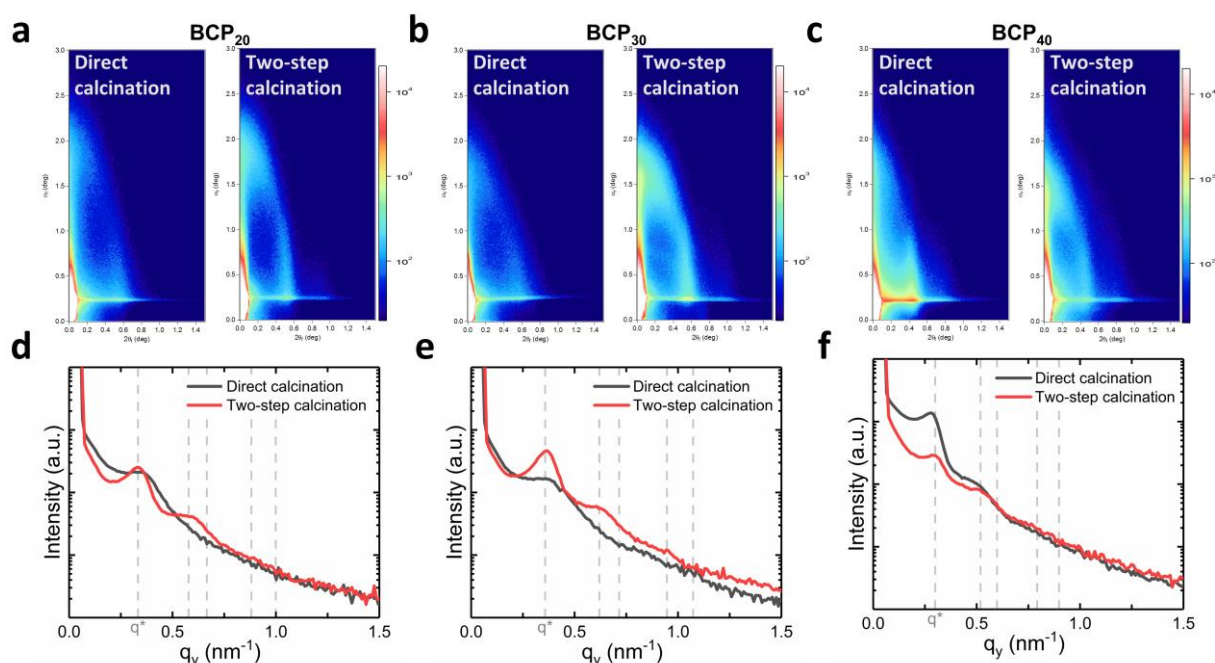


Figure 4 Thin film characterization by GISAXS of the films BCP₂₀ (a, d), BCP₃₀ (b, e), and BCP₄₀ (c, f) of PIB-*b*-PEO. 2D GISAXS scattering patterns (a-c) and the in-plane GISAXS line cuts (d-f), q_y , of samples directly calcined in air and after the two-step calcination. Dashed lines correspond to the expected peak positions of a hexagonal close-packed pore arrangement (q/q^* : 1, $\sqrt{3}$, $\sqrt{4}$, $\sqrt{7}$, and $\sqrt{9}$).

In a perfectly ordered 3D HCP configuration, the mesopore layers are stacked in an ABA' sequence.^[57] This configuration can, for example, maximize the diffusion of small molecules through the structure, since a pore in the reference plane B connects to 6 pores, three to the top

layer A and three to the bottom layer A'. Thus, it is reasonable to assume that the higher degree of order obtained by two-step calcination entails improved accessibility of the porous network with a higher number of percolation paths, beneficial for diffusion related applications. **Table 2** summarizes the in-plane center-to-center distance (D_{C-C}), out-of-plane D_{C-C} , Scherrer domain size, and extent of order calculated from the GISAXS patterns.

Table 2 Thin film structural parameters obtained by analysis of the GISAXS patterns.

Sample	Calcination process	First Bragg peak q^* [nm^{-1}]	in-plane D_{C-C} [nm]	out-of-plane D_{C-C} [nm]	Scherrer domain size D_{Sch} [nm]	Extent of order [pores]
BCP ₂₀	Two-step	0.333	18.9	5.0	63.9	3.4
BCP ₂₀	Direct	0.352	17.9	5.3	56.8	3.2
BCP ₃₀	Two-step	0.358	17.6	6.0	60.5	3.4
BCP ₃₀	Direct	0.373	16.8	5.3	51.6	3.1
BCP ₄₀	Two-step	0.299	21.0	7.1	86.9	4.2
BCP ₄₀	Direct	0.277	22.6	5.4	88.0	3.9

SEM micrographs of the thin films' top surface confirmed the structural pore arrangement, in-plane D_{C-C} and pore size obtained by EEP and GISAXS, as shown in **Figure 5**. In order to evaluate the mesoporous arrangement of the samples, SEM micrographs were analyzed with the software CORDERLY^[58] to obtain the spatial distribution function (SDF), an alternative measure for 2D structural order with distinct advantages over the standard 2D fast Fourier transform (FFT) in cases of limited periodicity (see Supplementary Information Figure S5 for the corresponding 2D FFT). The higher number of concentric hexagonal rings displayed in the 2D SDF (Figure 5 insets) of the two-step calcined samples suggests that the pores on the film surface exhibit a higher degree of HCP order in comparison to samples calcined directly in air, which in line with previous GISAXS observations.

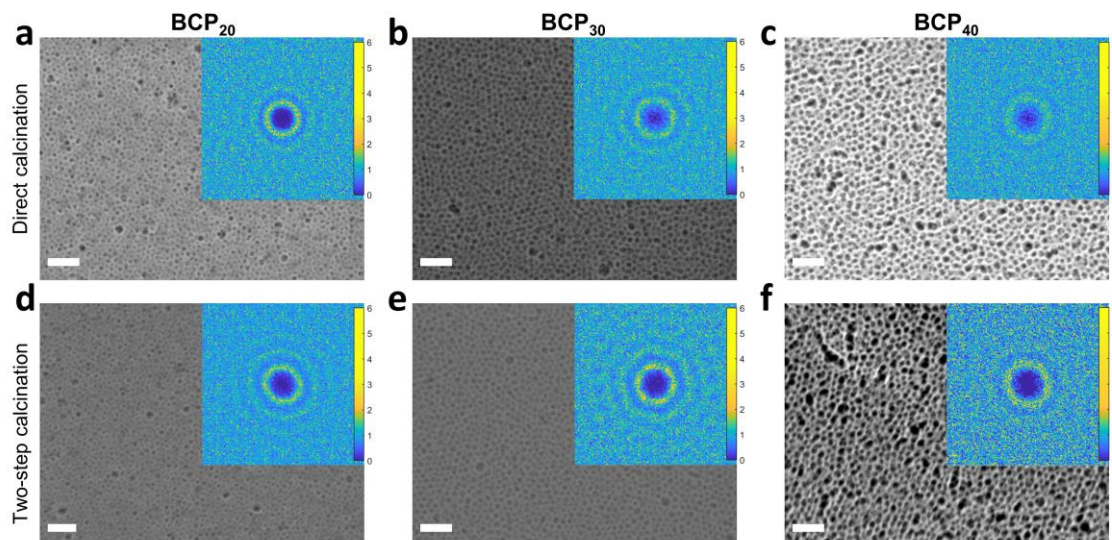


Figure 5 SEM images of the mesoporous films after direct calcination in air (a-c) and after the two-step calcination (d-f) process. The inset corresponds to the 2D spatial distribution function to evaluate pore ordering. Scale bar: 100 nm.

Higher magnification SEM micrographs (Supplementary Information Figure S6) revealed the interconnected nature of the mesoporous structure. We also noticed that the surface of the mesoporous films fabricated by either direct or two-step calcination was homogeneous and crack-free for the film thicknesses studied herein (< 200 nm after calcination). Table S1 summarizes the structural parameters obtained from the analysis of the SEM images and Figure S7 (Supplementary Information) displays the original SEM images.

2.5. Electrochemical characterization of the mesoporous thin films

Characterizing the material surface charge at a given pH is important for applications involving the mobility of charged molecules within the porous network, such as in protein physisorption or ion-exchange membranes.^[59–61] To identify the material surface charge and the effect of the two-step calcination in the charge transfer resistance (R_{ct}) of the films, we fabricated mesoporous films on electrically conductive FTO coated glass and measured cyclic voltammetry (CV) and electrochemical impedance spectroscopy (EIS), respectively. To this

end, redox probes with opposite electric charge were studied: the cationic redox active species $[\text{Ru}(\text{NH}_3)_6]^{2/3+}$ and the anionic redox couple $[\text{Fe}(\text{CN})_6]^{3/4-}$, both prepared in PBS buffer (pH 7.3), as shown in **Figure 6** for a BCP₄₀ film.

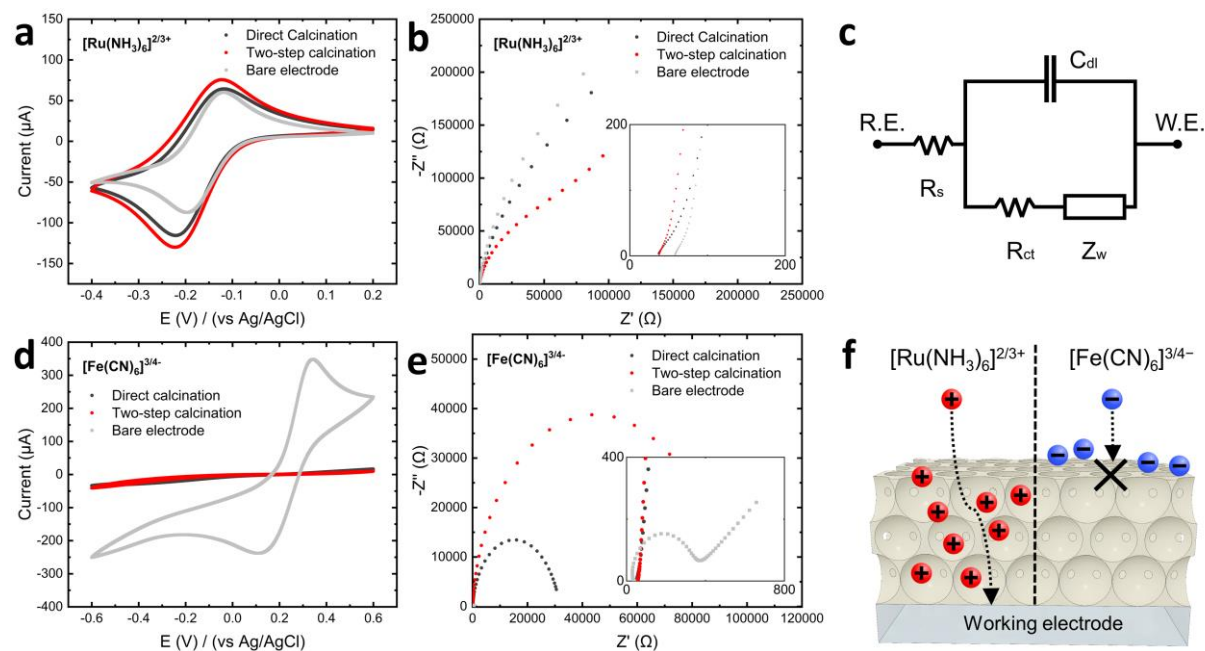


Figure 6 Electrochemical characterization of BCP₄₀ mesoporous thin films. Cyclic voltammogram (a,d) and Nyquist plot (b,e) measured using redox probes with opposite electric charge: (a,b) $[\text{Ru}(\text{NH}_3)_6]^{2/3+}$ and (d,e) $[\text{Fe}(\text{CN})_6]^{3/4-}$. c) Randles circuit used to fit the Nyquist plots. F) Schematic of the permselective behavior of the mesoporous thin film fabricated onto a FTO coated glass.

Cyclic voltammograms of the positively charged probe $[\text{Ru}(\text{NH}_3)_6]^{2/3+}$ (Figure 6a) show a similar electrochemical activity on the mesoporous films in comparison to a bare FTO glass electrode. A smaller peak-to-peak potential difference ($\Delta E_p = |E_{\text{oxidation}} - E_{\text{reduction}}|$) was obtained for two-step calcined films (ΔE_p 99 mV), indicating a faster and more reversible electrochemical response than for directly calcined films (ΔE_p 105 mV). The reference value for bare FTO glass was significantly lower (ΔE_p 79 mV). The improved electrochemical response of two-step calcined films may be directly related to the higher number of diffusion paths present in the structure in comparison to directly calcined films. The reversibility of the

CV also confirms that the mesoporous network interconnects the film's outer surface with the conductive substrate, in consequence discarding problems related to the substrate interface by preferential BCP wetting.^[62] We fitted a Randles circuit (Figure 6c) to the Nyquist plot obtained for EIS measurements. The charge transfer resistance (R_{ct}) of the two-step calcined films (2.4 Ω) was similar to directly calcined films (4.1 Ω) and to the base FTO glass (3.5 Ω) for the $[\text{Ru}(\text{NH}_3)_6]^{2/3+}$ redox pair. In contrast, the CV scan of the $[\text{Fe}(\text{CN})_6]^{3/4-}$ (Figure 6d) shows limited electrochemical activity for both, two-step and directly calcined films, compared to the bare FTO glass. Accordingly, EIS measurements (Figure 6e) showed a higher R_{ct} for two-step calcined films (87420 Ω) and directly calcined films (29730 Ω) than for a bare FTO electrode (310 Ω) in the presence of the negatively charged electrolyte. Analogous results were obtained for BCP₂₀ and BCP₃₀ thin films (see Supplementary Information Figure S8 and Figure S9). The permselective behavior towards positive charges evidences the mesoporous material is negatively charged at pH 7.3, attracting positive charges and repelling the negative electrolyte, as schematized in Figure 6f. Similar surface charge has been reported in aluminosilicates at pH 3-9, where the higher the silicon content, the lower was the pH of the isoelectric point.^[63] The source of the negative charge has been attributed to the deprotonation of the superficial silanol groups at pH >2.^[64] We also noticed that two-step calcined films had a higher R_{ct} than air-calcined films in presence of $[\text{Fe}(\text{CN})_6]^{3/4-}$. We attribute the difference in the charge transfer resistance to remnant carbon species that are not removed by air calcination and possess a negative surface charge.^[27,65] The improved permselective behavior obtained after the two-step process makes the mesoporous material an ideal candidate for ion-exchange membranes and enzyme storage applications.

2.6. Enzyme storage application

To study the effect of the mesoporous structure obtained by two-step calcination in applications requiring an accessible porosity, we measured enzyme physisorption into the mesoporous films using a quartz crystal microbalance (QCM). Lysozyme, a globular protein with enzymatic and antimicrobial properties,^[66] was chosen as a model system since it is positively charged at pH 7.3 (isoelectric point $pI=11$)^[59] and exhibits suitable dimensions ($3.0 \times 3.0 \times 4.5 \text{ nm}^3$)^[60] for the herein studied mesoporous architecture. To this end, we prepared BCP₄₀ mesoporous films onto silica coated QCM sensors and measured the frequency changes when exposed to 2 mg ml^{-1} of lysozyme in PBS buffer, as shown in **Figure 7b**. We then related the frequency changes to the enzyme mass using the Sauerbrey equation,^[67] as illustrated in Figure 7c.

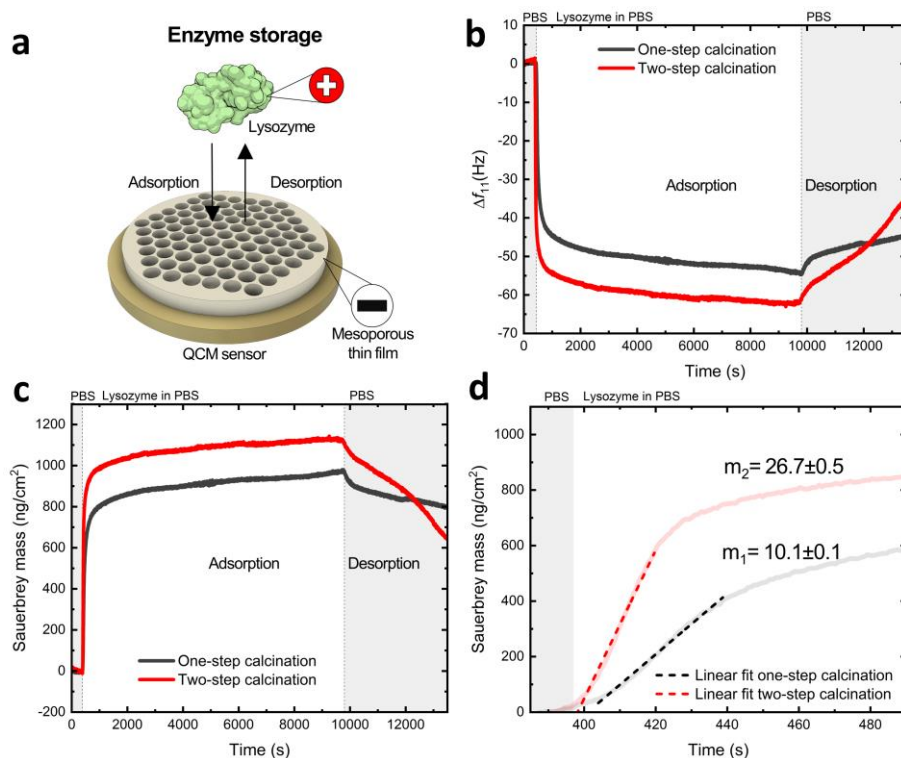


Figure 7 a) Schematic of lysozyme physisorption into mesopores measured by QCM. b) Frequency changes and c) enzyme mass adsorbed into the films. d) First minute of lysozyme adsorption into the films.

We found that two-step calcined films adsorbed more lysozyme (1116 ng cm^{-2}) than one-step calcined films (976 ng cm^{-2}) after 2.5 h of exposure to the enzyme-rich solution. The adsorbed mass difference ($\sim 13\%$) was proportional to the porosity difference of the films ($\sim 12\%$) (See Supplementary Information Figure S10). This observation is in good agreement with previous studies showing that protein loading efficiency increases with pore volume in mesoporous silica materials.^[68,69] Figure 7d shows the first minute of enzyme adsorption in the films. The faster adsorption kinetics observed in two-step calcined films (slope $m_2=26.7\pm 0.5$) with respect to one-step calcined films (slope $m_1=10.1\pm 0.1$), corroborate the improved pore connectivity and pore access obtained with the two-step fabrication protocol. Interestingly, two-step calcined films desorbed about 2.5x more enzyme (465 ng cm^{-2}) than directly calcined films (178 ng cm^{-2}) after 1 h of rinsing with PBS buffer. These findings provide evidence that the improved structural order with respect to pore shape and pore interconnectivity, enhances the accessibility to the porous network. The less restricted porous structures obtained in two-step calcined films allow to overcome the attractive electrostatic interaction between lysozyme and the aluminosilicate surface, easing protein desorption by concentration gradients and protein-protein repulsion forces. The ability to store and release an enzyme from the mesoporous structure is important for various use cases such as in antibacterial agents,^[70] glucose sensors,^[71] and biocatalysts.^[72] In consequence, processing mesoporous films at high temperature in argon prior to air calcination offers a clear benefit for these applications.

3. Conclusion

We have demonstrated that a two-step calcination protocol, composed of high-temperature treatment in argon, followed by air calcination, reduces uniaxial contraction of inorganic mesoporous thin films fabricated by supramolecular co-assembly in comparison with the common protocol involving air calcination immediately after film deposition.

The two-step calcined mesoporous films retain higher porosity, have a larger and more uniform pore size, and exhibit an improved hexagonally closed-packed order than one-step calcined films, as demonstrated here for a wide range of organic/inorganic ratios and two block copolymers (PIB-*b*-PEO, PI-*b*-PEO). While uniaxial shrinkage occurs in direct air calcination protocols due to the concurrent sol-gel condensation and early degradation of the organic BCP host, the herein proposed fabrication method allows retaining the structural support of the carbonized organic host during the sol-gel condensation. In consequence, the mesoporous architectures obtained by a two-step calcination display enhanced mass transport properties, demonstrated here for the adsorption and desorption of lysozyme as an example of enzyme storage but offering favorable performance in a broad range of applications.

4. Experimental Section

Reagents: PIB₃₉-*b*-PEO₃₆ block copolymer (polydispersity 1.26, M_n 4.85 kg mol⁻¹) was provided by BASF. Toluene (99.9%), 1-butanol (99.4%), aluminium tri-sec-butoxide (97%), (3-glycidyloxypropyl)-trimethoxysilane (GLYMO) (≥98%), potassium chloride (KCl) (≥99.9%), hexa ammine ruthenium (III) chloride [Ru(NH₃)₆]Cl₃ (98%) and lysozyme from chicken egg white (lyophilized powder, protein ≥90% , ≥40,000 units/mg protein) were purchased from Sigma-Aldrich. Poly(1,4-isoprene)-*b*-poly(ethylene oxide) block copolymer (polydispersity: 1.01, M_n PI(48)-*b*-PEO(12) kg mol⁻¹) was purchased from Polymer Source Inc. Potassium ferricyanide K₃[Fe(CN)₆] (99+%) was purchased from ACROS Organics. Potassium ferrocyanide K₄[Fe(CN)₆] (>98.5%) was purchased from Honeywell. Phosphate buffered saline (PBS) in tablets was purchased from OXOID. All chemicals were used without further purification.

Preparation of aluminosilicate sol-gel stock solution: the aluminosilicate stock solution was prepared by mixing and stirring in an ice bath 0.32 g of aluminium tri-sec-butoxide, 2.8 g of

GLYMO, and 20 mg of KCl. After 15 min of stirring, 0.135 ml of a 10 mM HCl solution was added dropwise to start the hydrolysis of the precursors and left for another 15 min in the ice bath. The mixture was then removed from the ice bath and stirred at room temperature for 15 min. 0.85 ml of 10 mM HCl was added to the solution and left stirring for 20 min to complete the hydrolysis. The final solution was filtered with a 0.2 μm cellulose syringe filter and dissolved with 2.135 ml of toluene/1-butanol (72.84/27.16 wt%) to get to a concentration of 1 g ml⁻¹ of aluminosilicate. The mixture was then kept refrigerated at 5 °C.

Preparation of the block copolymer stock solution: PIB-b-PEO received from BASF was dissolved in an azeotrope solution of toluene/1-butanol (72.84/27.16 wt%) in a concentration of 32 mg ml⁻¹ and subsequently filtered with a 0.2 μm cellulose syringe filter. PI-b-PEO was dissolved in an azeotropic solution of toluene/1-butanol (72.84/27.16 wt%) in a concentration of 40 mg ml⁻¹ and used without further filtration.

Fabrication of mesoporous aluminosilicate thin films by block copolymer co-assembly: First, the BCP stock solution was mixed with the aluminosilicate sol-gel stock solution in volumes described in **Table 3** producing the so-called hybrid solution and left mixing in a shaker for 30 min prior to use. 30 μl of the hybrid solution was spin-coated (2000 rpm, 20 s, Laurell WS 650 MZ) onto silicon, silica-coated QCM sensors (5 MHz 14 mm Cr/Au/SiO₂, Quartz PRO), FTO coated glass (TEC 6, Pilkington) or Au coated silicon substrates to generate the thin films. All substrates were plasma-treated in oxygen prior to deposition (300 s, 100 W, 0.33 mbar, Diener Electronic “Pico”) to activate the surface and remove organic contaminants. Thin films were subsequently calcined. “One-step calcination” films were calcined in air at 450 °C (30 minutes, 5 °C min⁻¹). “Two-step calcination” films were first annealed in argon at 450 °C (30 minutes, 5 °C min⁻¹) in a tubular furnace, and subsequently air calcined at 450 °C (30 minutes, 5 °C min⁻¹). All films were let cooled down inside the furnace.

Table 3 Block copolymer and aluminosilicate volumes used to generate a hybrid solution with BCP content of 20, 30 and 40%.

Sample	Block copolymer	Block copolymer content [% mass]	BCP stock solution [μ l]	Aluminosilicate stock solution [μ l]
BCP ₂₀	PIB- <i>b</i> -PEO	20	469	120
BCP ₃₀	PIB- <i>b</i> -PEO	30	469	70
BCP ₄₀	PIB- <i>b</i> -PEO	40	469	45
BCP ₂₀ [*]	PI- <i>b</i> -PEO	20	375	120
BCP ₃₀ [*]	PI- <i>b</i> -PEO	30	375	70
BCP ₄₀ [*]	PI- <i>b</i> -PEO	40	375	45

Fourier Transform Infrared Spectroscopy: FTIR spectra were measured in reflection mode on thin films fabricated onto Au coated silicon substrates using an AIM-9000 infrared microscope coupled with an IRTracer-1000 FTIR spectrophotometer (Shimadzu). Atmospheric and baseline correction were performed with the software Lab Solutions IR (Shimadzu).

Raman spectroscopy: Raman spectroscopy study was carried out using a Renishaw 1000 spectrometer equipped with a 633 nm laser (1.9eV, 1.0mW) and coupled to a microscope with 50x lens. The Raman system was calibrated using a silicon reference.

Spectroscopic ellipsometry (SE) and environmental ellipsometric porosimetry (EEP): SE and EEP were measured on mesoporous films deposited onto silicon substrates in a Semilabs SE2000 ellipsometer. Film thickness was measured at an incident angle of 73°. *In situ* spectroscopic ellipsometry was carried out at an incident angle of 65° in a customized chamber that allows thermal and atmosphere control.^[73] A flow controller (model F-201CV, Bronkhorst) was used to flow argon into the chamber (0.1 l min⁻¹). The integrated SEA software (Semilabs) was used to fit the experimental data for thickness using a Cauchy dispersion law, water volume adsorbed using the Lorentz-Lorentz effective medium approximation, and pore size distribution using the modified Kelvin equation. The pore size distribution error was calculated as the standard deviation of a Gaussian fit of the distribution.

Grazing-incidence small-angle scattering (GISAXS): GISAXS was performed in a Ganesha 300XL (Xenocs SAXSLAB) instrument on mesoporous films deposited onto silicon substrates, by employing a high brilliance microfocus Cu-source ($\lambda = 1.5418 \text{ \AA}$). The incidence angle was set at 0.2° . 2D GISAXS scattering patterns were collected using a PILATUS 300K solid-state photon-counting detector at a sample-to-detector distance of 950 mm. GISAXS data analysis was performed using FitGISAXS^[74] software.

Scanning electron microscopy (SEM): SEM images were taken in a Xbeam 540 FIB/SEM (ZEISS) directly on aluminosilicate mesoporous films without any metallic coating. Images were captured using an acceleration voltage between 0.5 to 2 kV and working distance between 0.9 to 1 mm. The 2D spatial distribution function was calculated with the software CORDERLY.^[58]

Electrochemical measurements: Cyclic voltammetry (potential range $[\text{Ru}(\text{NH}_3)_6]^{2/3+}$: -0.4 to 0.2 V; potential range $[\text{Fe}(\text{CN})_6]^{3/4-}$: -0.6 to 0.6 V; scan rate 100 mV S^{-1}) and electrochemical impedance spectroscopy (frequency range: 0.1 Hz to 100 kHz, amplitude 5 mV) were measured with a potentiostat (Reference 600+, Gamry) in a 3-electrode set-up. The reference, counter, and working electrode were Ag/AgCl, a platinum wire (0.4 mm diameter) and FTO coated glass containing the mesoporous film (area: 0.5 cm^2), respectively. The negatively charged electrolyte $[\text{Fe}(\text{CN})_6]^{3/4-}$ was a mixture of 2 mM potassium ferrocyanide and 2 mM potassium ferricyanide in 0.1 M PBS. The positively charged electrolyte $[\text{Ru}(\text{NH}_3)_6]^{2/3+}$ was 1 mM hexaammineruthenium(III) chloride in 0.1 M PBS. Measurements were analyzed and fitted with the software Gamry Echem Analyst.

Enzyme storage: Enzyme storage was studied with a quartz crystal microbalance (Q-Sense E4 instrument, Biolin Scientific) on mesoporous films prepared onto silica-coated QCM sensors (5 MHz 14 mm Cr/Au/SiO₂, Quartz PRO) with an active area of 0.79 cm^2 . Lysozyme and PBS

were pumped into the QCM chamber at a flow rate of 30 $\mu\text{l min}^{-1}$. Frequency analysis and conversion to Sauerbrey mass were performed with the software QTools (Biolin Scientific).

Supporting Information

Supporting Information is available as a separate file.

Acknowledgements

MJF, AAF and SG are grateful for funding by an EPSRC New Investigator award (EP/R035105/1). MJF wish to acknowledge the support of the Henry Royce Institute through the Royce PhD Equipment Access Scheme enabling access to microscopy facilities at Royce@Cambridge; EPSRC Grant Number EP/R00661X/1. This work used the Melbourne Centre for Nanofabrication (MCN) in the Victorian Node of the NCRIS-enabled Australian National Fabrication Facility (ANFF).

References

- [1] T. Waitz, T. Wagner, T. Sauerwald, C. D. Kohl, M. Tiemann, *Adv. Funct. Mater.* **2009**, *19*, 653.
- [2] L. G. Teoh, Y. M. Hon, J. Shieh, W. H. Lai, M. H. Hon, *Sensors Actuators, B Chem.* **2003**, *96*, 219.
- [3] M. Mamak, N. Coombs, G. A. Ozin, *Adv. Funtional Mater.* **2001**, *11*, 59.
- [4] H. Chang, S. H. Joo, C. Pak, *J. Mater. Chem.* **2007**, *17*, 3078.
- [5] M. C. Fuertes, F. J. López-Alcaraz, M. C. Marchi, H. E. Troiani, V. Luca, H. Míguez, G. J. D. A. A. Soler-Illia, *Adv. Funct. Mater.* **2007**, *17*, 1247.
- [6] D. Fattakhova-Rohlfing, M. Wark, J. Rathouský, *Chem. Mater.* **2007**, *19*, 1640.
- [7] A. K. Chandiran, P. Comte, R. Humphry-Baker, F. Kessler, C. Yi, M. K. Nazeeruddin, M. Grätzel, *Adv. Funct. Mater.* **2013**, *23*, 2775.
- [8] M. Nedelcu, J. Lee, E. J. W. Crossland, S. C. Warren, M. C. Orilall, S. Guldin, S. Hüttner,

- C. Ducati, D. Eder, U. Wiesner, U. Steiner, H. J. Snaith, *Soft Matter* **2009**, 5, 134.
- [9] A. Vu, Y. Qian, A. Stein, *Adv. Energy Mater.* **2012**, 2, 1056.
- [10] J. Haetge, C. Suchomski, T. Brezesinski, *Small* **2013**, 9, 2541.
- [11] W. Li, J. Liu, D. Zhao, *Nat. Rev. Mater.* **2016**, 1, 16023.
- [12] C. X. Guo, C. M. Li, *Adv. Funct. Mater.* **2016**, 26, 8824.
- [13] A. Y. Khan, S. B. Noronha, R. Bandyopadhyaya, *Biochem. Eng. J.* **2014**, 91, 78.
- [14] M. Thust, M. J. Schöning, S. Frohnhoff, R. Arens-Fischer, P. Kordos, H. Lüth, *Meas. Sci. Technol.* **1996**, 7, 26.
- [15] D. R. Rolison, *Science (80-.)*. **2003**, 299, 1698.
- [16] P. Innocenzi, L. Malfatti, *Chem. Soc. Rev.* **2013**, 42, 4198.
- [17] B. Reid, A. Alvarez-Fernandez, B. Schmidt-Hansberg, S. Guldin, *Langmuir* **2019**, 35, 14074.
- [18] A. Alvarez-Fernandez, B. Reid, J. Suthar, S. Y. Choy, M. Jara Fornerod, N. Mac Fhionnlaoich, L. Yang, B. Schmidt-Hansberg, S. Guldin, *Nanoscale* **2020**, 12, 18455.
- [19] V. N. Urade, T. C. Wei, M. P. Tate, J. D. Kowalski, H. W. Hillhouse, *Chem. Mater.* **2007**, 19, 768.
- [20] A. Sarkar, A. Thyagarajan, A. Cole, M. Stefik, *Soft Matter* **2019**, 15, 5193.
- [21] K. A. Lantz, N. B. Clamp, W. van den Bergh, A. Sarkar, M. Stefik, *Small* **2019**, 15, 1900393.
- [22] H. N. Lokupitiya, A. Jones, B. Reid, S. Guldin, M. Stefik, *Chem. Mater.* **2016**, 28, 1653.
- [23] Y. J. Cheng, J. S. Gutmann, *J. Am. Chem. Soc.* **2006**, 128, 4658.
- [24] L. L. Hench, J. K. West, *The Sol-Gel Process*, Vol. 90, **1990**.
- [25] C. J. Brinker, G. W. Scherer, *Sol-Gel Science: The Physics and Chemistry of Sol-Gel Processing*, Elsevier Inc., **2013**.
- [26] A. Alvarez-Fernandez, B. Reid, M. J. Fornerod, A. Taylor, G. Divitini, S. Guldin, *ACS*

- Appl. Mater. Interfaces* **2020**, *12*, 5195.
- [27] P. Mohapatra, S. Shaw, D. Mendivelso-Perez, J. M. Bobbitt, T. F. Silva, F. Naab, B. Yuan, X. Tian, E. A. Smith, L. Cademartiri, *Nat. Commun.* **2017**, *8*, 1.
 - [28] C. Boissiere, D. Grosso, S. Lepoutre, L. Nicole, A. B. Bruneau, C. Sanchez, *Langmuir* **2005**, *21*, 12362.
 - [29] M. Kuemmel, D. Grosso, C. Boissière, B. Smarsly, T. Brezesinski, P. A. Albouy, H. Amenitsch, C. Sanchez, *Angew. Chemie* **2005**, *117*, 4665.
 - [30] S. Wang, P. Tangvijitsakul, Z. Qiang, S. M. Bhaway, K. Lin, K. A. Cavicchi, M. D. Soucek, B. D. Vogt, *Langmuir* **2016**, *32*, 4077.
 - [31] X. Jiang, H. Oveisi, Y. Nemoto, N. Suzuki, K. C. W. Wu, Y. Yamauchi, *Dalt. Trans.* **2011**, *40*, 10851.
 - [32] S. Y. Choi, B. Lee, D. B. Carew, M. Mamak, F. C. Peiris, S. Speakman, N. Chopra, G. A. Ozin, *Adv. Funct. Mater.* **2006**, *16*, 1731.
 - [33] J. Haetge, P. Hartmann, K. Brezesinski, J. Janek, T. Brezesinski, *Chem. Mater.* **2011**, *23*, 4384.
 - [34] K. Brezesinski, J. Wang, J. Haetge, C. Reitz, S. O. Steinmueller, S. H. Tolbert, B. M. Smarsly, B. Dunn, T. Brezesinski, *J. Am. Chem. Soc.* **2010**, *132*, 6982.
 - [35] T. Brezesinski, J. Wang, R. Senter, K. Brezesinski, B. Dunn, S. H. Tolbert, In *ACS Nano*, American Chemical Society, **2010**, pp. 967–977.
 - [36] C. Revenant, M. Benwadih, *Thin Solid Films* **2016**, *616*, 643.
 - [37] R. E. Williford, R. S. Addleman, X. S. Li, T. S. Zemanian, J. C. Birnbaum, G. E. Fryxell, *J. Non. Cryst. Solids* **2005**, *351*, 2217.
 - [38] J. R. Casanova, E. A. Heredia, C. D. Bojorge, H. R. Cánepa, G. Kellermann, A. F. Craievich, *Appl. Surf. Sci.* **2011**, *257*, 10045.
 - [39] S. Guldin, P. Docampo, M. Stefik, G. Kamita, U. Wiesner, H. J. Snaith, U. Steiner, *Small*

- 2012**, 8, 432.
- [40] S. Dutta, K. C.-W. Wu, T. Kimura, *Chem. Mater.* **2015**, 27, 6918.
 - [41] W. Chen, Y. Geng, X. D. Sun, Q. Cai, H. De Li, D. Weng, *Microporous Mesoporous Mater.* **2008**, 111, 219.
 - [42] J. Lee, M. Christopher Orilall, S. C. Warren, M. Kamperman, F. J. Disalvo, U. Wiesner, *Nat. Mater.* **2008**, 7, 222.
 - [43] S. M. De Paul, J. W. Zwanziger, R. Ulrich, U. Wiesner, H. W. Spiess, *J. Am. Chem. Soc.* **1999**, 121, 5727.
 - [44] B. Reid, A. Taylor, A. Alvarez-Fernandez, M. H. Ismael, S. Sharma, B. Schmidt-Hansberg, S. Guldin, *ACS Appl. Mater. Interfaces* **2019**, 11, 19308.
 - [45] B. Reid, A. Taylor, Y. Chen, B. Schmidt-Hansberg, S. Guldin, *ACS Appl. Mater. Interfaces* **2018**, 10, 10315.
 - [46] C. Liang, K. Hong, G. A. Guiochon, J. W. Mays, S. Dai, *Angew. Chemie - Int. Ed.* **2004**, 43, 5785.
 - [47] S. Guldin, P. Kohn, M. Stefik, J. Song, G. Divitini, F. Ecarla, C. Ducati, U. Wiesner, U. Steiner, *Nano Lett.* **2013**, 13, 5329.
 - [48] M. Berta, C. Lindsay, G. Pans, G. Camino, *Polym. Degrad. Stab.* **2006**, 91, 1179.
 - [49] M. Zanetti, G. Camino, P. Reichert, R. Mülhaupt, *Macromol. Rapid Commun.* **2001**, 22, 176.
 - [50] M. Zanetti, P. Bracco, L. Costa, *Polym. Degrad. Stab.* **2004**, 85, 657.
 - [51] A. Laachachi, E. Leroy, M. Cochez, M. Ferriol, J. M. Lopez Cuesta, *Polym. Degrad. Stab.* **2005**, 89, 344.
 - [52] M. Thommes, K. Kaneko, A. V Neimark, J. P. Olivier, F. Rodriguez-Reinoso, J. Rouquerol, K. S. W. Sing, *Pure Appl. Chem.* **2015**, 87, 1051.
 - [53] M. R. Baklanov, K. P. Mogilnikov, V. G. Polovinkin, F. N. Dultsev, *J. Vac. Sci. Technol.*

- B Microelectron. Nanom. Struct.* **2000**, *18*, 1385.
- [54] A. Hexemer, P. Müller-Buschbaum, *IUCrJ* **2015**, *2*, 106.
- [55] I. W. Hamley, V. Castelletto, *Prog. Polym. Sci.* **2004**, *29*, 909.
- [56] D.-M. Smilgies, *J. Appl. Crystallogr.* **2009**, *42*, 1030.
- [57] Y. Ma, L. Han, K. Miyasaka, P. Oleynikov, S. Che, O. Terasaki, *Chem. Mater.* **2013**, *25*, 2184.
- [58] N. Mac Fhionnlaoich, R. Qi, S. Guldin, *Langmuir* **2019**, *35*, 16605.
- [59] L. C. Sang, A. Vinu, M. O. Coppens, *Langmuir* **2011**, *27*, 13828.
- [60] L. C. Sang, M. O. Coppens, *Phys. Chem. Chem. Phys.* **2011**, *13*, 6689.
- [61] D. Fattakhova-Rohlfing, M. Wark, J. Rathouský, *Chem. Mater.* **2007**, *19*, 1640.
- [62] P. Sutton, P. Bennington, S. N. Patel, M. Stefik, U. B. Wiesner, P. F. Nealey, U. Steiner, I. Gunkel, *Adv. Funct. Mater.* **2019**, *29*, 1905977.
- [63] K. W. Perrott, *Clays Clay Miner.* **1977**, *25*, 417.
- [64] B. M. Lowe, C.-K. Skylaris, N. G. Green, *J. Colloid Interface Sci.* **2015**, *451*, 231.
- [65] J. H. Bae, D. Wang, K. Hu, M. V. Mirkin, *Anal. Chem.* **2019**, *91*, 5530.
- [66] D. M. Chipman, N. Sharon, *Mechanism of lysozyme action*, Vol. 165, American Association for the Advancement of Science, **1969**, pp. 454–465.
- [67] G. Sauerbrey, *Zeitschrift für Phys.* **1959**, *155*, 206.
- [68] M. Miyahara, A. Vinu, K. Z. Hossain, T. Nakanishi, K. Ariga, In *Thin Solid Films*, Elsevier, **2006**, pp. 13–18.
- [69] M. Miyahara, A. Vinu, K. Ariga, *Mater. Sci. Eng. C* **2007**, *27*, 232.
- [70] L. li Li, H. Wang, *Adv. Healthc. Mater.* **2013**, *2*, 1351.
- [71] G. Zhou, K. K. Fung, L. W. Wong, Y. Chen, R. Renneberg, S. Yang, *Talanta* **2011**, *84*, 659.
- [72] Z. Zhou, M. Hartmann, *Chem. Soc. Rev.* **2013**, *42*, 3894.

- [73] S. Hüttner, M. Sommer, A. Chiche, G. Krausch, U. Steiner, M. Thelakkat, *Soft Matter* **2009**, 5, 4206.
- [74] D. Babonneau, *J. Appl. Crystallogr.* **2010**, 43, 929.